Flinders
UNIVERSITY

Elastic and inelastic cross sections for low-energy electron collisions with pyrimidine

Zdeněk Mašín, Jimena D. Gorfinkiel, Darryl B. Jones, Susan M. Bellm, and Michael J. Brunger

Citation: J. Chem. Phys. **136**, 144310 (2012); doi: 10.1063/1.3702629
View online: http://dx.doi.org/10.1063/1.3702629
View Table of Contents: http://jcp.aip.org/resource/1/JCPSA6/v136/i14
Published by the American Institute of Physics.

Elastic and inelastic cross sections for low-energy electron collisions with pyrimidine

Zdeněk Mašín,[1,a)] Jimena D. Gorfinkiel,[1,b)] Darryl B. Jones,[2,c)] Susan M. Bellm,[2,d)] and Michael J. Brunger[2,3,e)]

[1]*Department of Physical Sciences, The Open University, Walton Hall, Milton Keynes, MK7 6AA, United Kingdom*
[2]*ARC Centre for Antimatter-Matter Studies, School of Chemical and Physical Sciences, Flinders University, GPO Box 2100, Adelaide, SA 5001, Australia*
[3]*Institute of Mathematical Sciences, University of Malaya, Kuala Lumpur 50603, Malaysia*

(Received 28 February 2012; accepted 26 March 2012; published online 12 April 2012)

We present theoretical elastic and electronic excitation cross sections and experimental electronic excitation cross sections for electron collisions with pyrimidine. We use the R-matrix method to determine elastic integral and differential cross sections and integral inelastic cross sections for energies up to 15 eV. The experimental inelastic cross sections have been determined in the 15–50 eV impact energy range. Typically, there is quite reasonable agreement between the theoretical and experimental integral inelastic cross sections. Calculated elastic cross sections agree very well with prior results. © *2012 American Institute of Physics*. [http://dx.doi.org/10.1063/1.3702629]

I. INTRODUCTION

Low energy electron collision data are available for a large number of molecular targets, although those data are often incomplete.[1] While integral and differential cross sections (ICS and DCS, respectively) have been measured and calculated with a variety of techniques, such data are generally only available for the elastic scattering channel. In contrast, electronic excitation data near the ionization threshold are scarce; this is the case both for theoretical and experimental cross sections.

Current computational implementations of the Kohn variational method,[2] the multichannel Schwinger method[3–5] and the R-matrix method[6] are able to provide electronically inelastic cross sections at low energies. Nonetheless, there are very few, if any, targets for which there is direct comparison between experiment and the *ab initio* calculations. Water[7] is one of the few systems for which a comparison of integral excitation cross sections has been made in the 20–50 eV range for several target states. No such comparison exists for larger molecules.

Three DNA/RNA bases, cytosine, thymine, and uracil, are pyrimidine derivatives (the other two, adenine and guanine, are substituted purine rings). Pyrimidine can therefore be used as a model molecule in studies, both theoretical and experimental, of electron scattering from DNA bases. The interest in low energy collisions between electron and DNA constituents stems from their importance in the radiation damage of biological systems. Electrons with energies below 20 eV are the most abundant secondary species produced by ionizing radiation. Experimental work has confirmed[8] that electrons with a few eV of energy are capable of breaking DNA strands; this process proceeds via the formation of temporary negative ions. Over the last decade, a number of experimental works on electron-DNA bases have been reported;[9,10] theoretical work is scarcer due to the computational requirements that calculations for these low-symmetry, electron-rich systems entail (particularly for *ab initio* methods). The experimental work has focused on providing information on the dissociative electron attachment (DEA) process, with data for elastic cross sections (and for electronic excitation in the condensed phase[11]) also available. On the theoretical side, studies have focused on providing elastic cross sections and information on the temporary negative ions that lead to DEA; only calculations for uracil[12,13] have reported inelastic cross sections.

Prior experimental work on electron collisions from pyrimidine includes the determination of absolute elastic differential cross sections,[14] above ionization energies (50–300 eV), and absolute differential and integral elastic cross sections in the 3–50 eV range.[15] Measurements have also been performed for condensed pyrimidine,[16] for which vibrational and electronic excitation cross sections were determined. Electron energy loss and VUV spectroscopy experiments[17,18] have provided insight into the electronic excited states of the molecule. Resonance formation in pyrimidine has also been studied experimentally, starting from the pioneering work of Nenner and Schulz.[19]

From the theoretical point of view, the Schwinger technique has been applied[15] to calculate elastic differential cross sections below 50 eV and the independent atom model has been used[20] to determine total and elastic integral cross sections up to 10 keV (the latter work also presents integral elastic cross sections for positron collisions for energies up to 45 eV).

In this paper, we present theoretical and experimental electronically inelastic cross sections for electron scattering

a)Electronic mail: z.masin@open.ac.uk.
b)Electronic mail: j.gorfinkiel@open.ac.uk.
c)Electronic mail: darryl.jones@flinders.edu.au.
d)Electronic mail: susan.bellm@flinders.edu.au.
e)Electronic mail: michael.brunger@flinders.edu.au.

from pyrimidine. Experimental cross sections are determined in the 15–50 eV energy range. Theoretical results, including elastic cross sections, are determined up to 15 eV. Calculations are performed at various levels of approximation; a close-coupling (CC) expansion method is employed to obtain integral electronically inelastic cross sections. In order to be accurate, a standard CC method, like the R-matrix method used in this work, requires the inclusion of all the energetically available target states in the expansion of the scattering wavefunction. Above the ionization threshold (around 9.7 eV in pyrimidine) this means, in principle, that ionized states of the target should be included. Although not impossible (for example, the molecular R-matrix with pseudostates method makes use of pseudostates to describe near-threshold ionization[21]), the current computational implementation of the codes puts it beyond our means for molecules of this size. In order to compare with experiment, we nonetheless present here calculated cross sections up to 15 eV. It should be understood that above around 10 eV, the highest energy for which we include states in the CC expansions, our calculated cross sections are intrinsically less accurate than those calculated at the lower energies.

Section II briefly summarizes the R-matrix method. Section III describes the experimental methodology and analysis techniques while Sec. IV presents the details of our calculations. Section V shows our calculated elastic (differential and integral) cross sections and compares them to available experimental and theoretical data. Section VI shows our results for inelastic scattering and finally, in Sec. VII, we present our conclusions.

II. THEORY

The R-matrix method and its application to electron-molecule scattering have been described in detail in Refs. 6, 22, and 23, so we only briefly summarize the method below. For our calculations, performed within the fixed-nuclei approximation, we have used the UKRmol suite.[24]

The basic idea of the R-matrix method is the division of the configuration space of the electron-molecule collision problem into two regions, separated by a sphere of radius $r = a$ large enough to enclose the whole charge density of the target states of interest.[25] In order to solve the scattering problem, we start by solving the more complex inner region problem. In this region, we can express the wavefunction for the N + 1 electron system as a linear combination

$$\Psi_k^{\Gamma}(\mathbf{X_1}....\mathbf{X_{N+1}}) = \mathcal{A}\sum_{i=1}^{n}\sum_{j=1}^{n_c}\Phi_i(\mathbf{X_1}....\mathbf{X_N};\hat{r}_{N+1};\sigma_{N+1}) \times \frac{u_{ij}(r_{N+1})}{r_{N+1}}a_{ijk} + \sum_{i=1}^{m}\chi_i(\mathbf{X_1}....\mathbf{X_{N+1}})b_{ik}, \quad (1)$$

where $\mathbf{X_i}$ represent the space and spin coordinates of electron i and $\sigma_{\mathbf{N+1}}$ indicates the spin coordinates of the (N + 1)th electron. The functions $\Phi_i(\mathbf{X_N};\hat{r}_{N+1};\sigma_{N+1})$ are built as products of the target wavefunctions $\Phi_i(\mathbf{X_N})$ of each of the n states included in the calculation and the angular (spherical harmonics) and spin functions of the scattering electron. The functions u_{ij} describe the radial behaviour of the scattering electron. They are generated from linear combinations of Gaussian functions centred on the centre of mass of the molecule. Finally, $\chi_i(\mathbf{X_{N+1}})$ are known as L^2-integrable functions and are built as products of molecular orbitals; they are crucial for the representation of short-range correlation and polarization effects. The spin-space symmetry of the wavefunctions is denoted by Γ. The operator $\mathcal{A}$ ensures the antisymmetrization of the whole wavefunction.

The coefficients a_{ijk} and b_{ik} are obtained by diagonalizing the fixed-nuclei N + 1 Hamiltonian.[26] In this way, we obtain a set of Ψ_k^{Γ} and their associated eigenvalues, E_k^{Γ}, that allow us to describe the N + 1 system in the inner region.

In the outer region, where $r \geq a$, exchange between the scattering and target electrons can be neglected: a single centre expansion of the electron-molecule interaction is used. In order to obtain scattering information, a set of coupled differential equations for the radial functions describing the behaviour of the scattering electron must be solved. This is done by propagating the R-matrix, constructed using inner region information (Ψ_k^{Γ} and E_k^{Γ}). This propagation is carried out to a radius large enough so that an asymptotic expansion for the radial wavefunctions of the scattering electron in each channel can be used. Finally, by matching these to known analytical asymptotic solutions, K-matrices containing the scattering information are obtained. Integral and differential cross sections, temporary negative ions' properties, etc. are derived from these.

III. EXPERIMENTAL METHOD AND ANALYSIS TECHNIQUE

Electron energy loss spectra (see Figure 1) have been measured using an apparatus based at Flinders University that has been fully described previously.[27] Briefly, a monochromated beam of 15–50 eV electrons, with a typical flux of 2–5 nA being detected in a Faraday cup, was incident on an orthogonal beam of pyrimidine molecules. Here, the molecular beam was created by allowing the vapour from a high purity pyrimidine sample (Sigma-Aldrich /Austin Chemical Company, >98.9% assay) to effuse through a 0.7 mm internal diameter capillary. Note that the pyrimidine sample underwent repeated freeze pump thaw cycles to remove any dissolved gases. The intersection of these beams defined a collision volume where the electrons interacted with the pyrimidine molecules. Electrons that collided with the molecules in the beam and scattered into the θ-direction (called the scattering angle) were energy analysed using a hemispherical selector before being detected with a channel electron multiplier. Experiments were performed with a chamber pressure typically of the order of 5×10^{-6} Torr, which ensured there were no multiple scattering events. Here, the combined instrumental energy resolution was of the order of 65 meV (FWHM). Energy loss spectra were accumulated at each scattering angle and incident electron energy by recording the number of scattered electrons detected at each energy loss value. The true electron count rate at each given energy loss was recorded

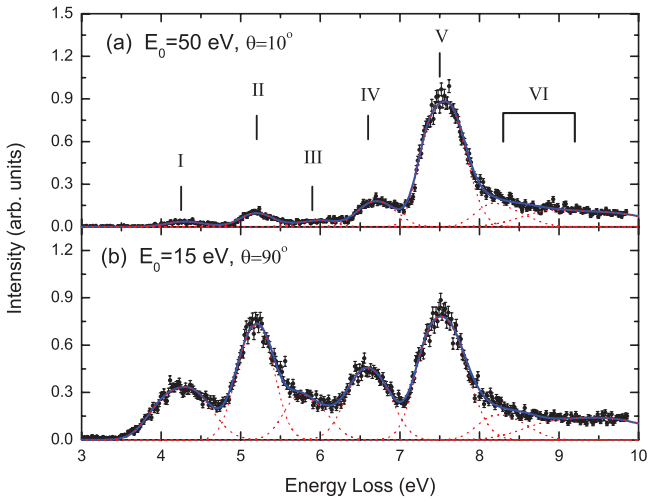

FIG. 1. Typical electron impact energy loss spectra measured for (a) $E_0 = 50$ eV and $\theta = 10^\circ$ and (b) $E_0 = 15$ eV and $\theta = 90^\circ$. For each spectrum, the spectral deconvolutions for each feature (dashed lines) and their sum (solid line) are also presented. The spectral assignments for each feature are also given in Table II. See text for full details.

using a multi-channel scaler synchronized to a linear voltage ramp that varied the detected electron energy loss between −0.5 and 9.8 eV. In this way, a given energy loss spectrum was built up by continually scanning over the range of energy loss values, thus minimizing variations due to changes in the target gas density and fluctuations in the incident beam current. Energy loss spectra at each incident energy and angle were repeatedly measured (2–4 times) to ensure reproducibility of the elastic to inelastic ratios (see below) to within the experimental uncertainty.

The respective energy loss spectra were next deconvolved into contributions arising from each individual or unresolved combination of electronic states. Examples of the deconvolution at two different scattering conditions are shown in Figure 1. Here, either 1 or 2 Gaussian functions were employed as fitting functions that approximated the spectral profiles observed over the range of scattering conditions covered in the experiments, for each resolvable inelastic feature and the elastic scattering peak. Note that the respective positions and widths of the Gaussian functions for each inelastic feature were established through consideration of the experimental photo-absorption spectra, previous electron energy loss spectra, and calculated electronic excitation energies.[17,28–31] The ratio of the area under the fitting function for the ith inelastic scattering feature to that found under the elastic feature determines the intensity ratio $\frac{I_i}{I_0}$ at that incident energy and scattering angle. The absolute differential cross sections for the inelastic processes contributing to the ith feature, $\frac{d\sigma_{i0}}{d\Omega}(E_0, \theta)$, can then be determined through

$$\frac{d\sigma_{i0}}{d\Omega}(E_0, \theta) = \frac{I_i}{I_0}\eta_{i0}\frac{d\sigma_0}{d\Omega}(E_0, \theta). \quad (2)$$

Here, $\frac{d\sigma_0}{d\Omega}(E_0, \theta)$ are the recently measured DCSs for elastic scattering from pyrimidine.[15] η_{i0} is the relative transmission efficiency of the analyser for inelastically and elastically scattered electrons. Following a similar procedure to Allan,[32] an additional focusing lens (synchronized to the voltage ramp) was also employed to minimise variations in transmission efficiency for electrons detected with different energy losses. Here, η_{i0} has been measured to be unity to within an uncertainty of 20%. DCS data for the most intense $\pi\pi^*$ excitations at two incident energies have been previously reported in a comparison with inelastic scattering from benzene.[33] A full discussion of the present DCS measurements will appear elsewhere. The measured inelastic DCSs are next converted into ICSs for each transition.

The DCS for a scattering process is related to the ICS, $\sigma_{i0}(E_0)$, for that process through the standard formula[1]

$$\sigma_{i0}(E_0) = 2\pi \int_0^\pi \frac{d\sigma_{i0}}{d\Omega}(E_0, \theta)\sin(\theta)\, d\theta. \quad (3)$$

In order to convert experimental DCS data, measured at discrete angles that span a finite angular range determined by the physical constraints of the apparatus, to an ICS, one must first extrapolate/interpolate the experimental data so that it covers the full angular range (0°–180°).[34] This has previously been accomplished through fitting an empirical function to the experimental data; as in molecular phase-shift analysis techniques.[35] However, by determining the ICS through a single optimised function there is no reliable method for estimating the uncertainty on the derived ICS value. This limits the effectiveness of such methods for calculating the ICS values from experimentally measured DCS data.

To overcome these limitations, we have developed a statistical weighting method for calculating ICSs. Here, instead of calculating the ICS from a single curve that approximates the DCS over all angles, we use multiple curves that span the one-standard deviation uncertainty range of the experimental data over the measured angular range. In this approach, each curve is generated to have constant statistical probability with respect to the experimental uncertainty. These lines are created by linearly interpolating the experimental data points at values where the statistical probability (determined from a Gaussian distribution) remains constant. In the case of DCS measurements over a finite angular range, the curves are then continued so that they extrapolate the data over the full angular range. Here, the end points used for the extrapolation are sequentially incremented so that they span a range of physically reasonable values, selectively determined for the scattering process of interest. The integration in Eq. (3) is then performed for each curve using numerical techniques. The calculated ICS for each curve is then assigned the statistical probability of where the curve intersected each of the experimental data points. By then fitting a Gaussian function to these probabilities, the peak position and its width give the best estimate of the ICS and its uncertainty, respectively. Hence, we avoid problems associated with fitting experimental data with a single function. Furthermore, the uncertainty of each experimental data point is explicitly included in the calculation of the ICS. Last, the uncertainty of any extrapolation is also included through the selection of appropriate extrapolation ranges. Thus, the derived ICS and its uncertainty accurately reflect the experimental uncertainty and the limitations employed in the extrapolation.

In the present ICS calculations, our DCSs are extrapolated to forward and backward angles so that the DCS values

at 0°–180° span the range from 0.2 times to 5 times the measured DCS value at the most forward or backward scattering angle. This represents our standard method for determining the ICS, with the calculated values being presented in Sec. VI (see Table III). However, we note that ICS determination for polar species has been particularly problematic.[36] For polar species, the ICS is often dominated by large contributions from the forward scattering angles which are not physically measured in the experiment. We have therefore improved our estimate of the ICS by adjusting the range of DCS (0°) values that specify our extrapolation to forward scattering angles. Here, we can estimate a more physical extrapolation based on the established analytic behaviour of the generalised oscillator strength (GOS) for dipole allowed transitions.

For electron impact excitation processes of dipole-allowed transitions, the experimental DCS are related to the GOS (in atomic units) for that transition,[37]

$$GOS_{i0} = \frac{1}{2} E_i \frac{k_i}{k_0} K^2 \frac{d\sigma_{i0}}{d\Omega}(E_0, \theta). \tag{4}$$

Here, k_0 and k_i are the magnitudes of the momentum of the incident and inelastically scattered electron, respectively. K is the magnitude of the momentum transferred in the scattering process and E_i is the excitation energy.

The study of the analytic properties of the GOS for a dipole-allowed excitation,[37,38] has led to a general analytic formula being proposed[39] to describe the GOS behaviour,

$$GOS(x) = \frac{1}{(1+x)^6}\left[\sum_{m=0}^{\infty} \frac{f_m x^m}{(1+x)^m}\right]. \tag{5}$$

Here, $x = K^2/\alpha^2$. The optimum model for the experimental GOS data (derived using Eq. (4) from the experimental DCS data) is generated by optimising the parameters, α and f_i, using a least-squares fitting technique. The quality of the fit can be checked against the optical oscillator strength for the transition, which the GOS approaches in the limit of K^2 goes to zero. This verification ensures that any forward angle extrapolation is realistic. The optimum fit to the GOS is then converted back to a DCS for the forward scattering angles. While this analysis procedure is not strictly applicable for each experimental feature (being composed of both dipole-allowed and spin-forbidden transition) at these low energies, the experimental DCS angular profiles, being dominated by strong forward scattering features (not shown), leads us to believe that this GOS analysis fitting procedure gives us a reasonable estimate of the DCS at forward scattering angles. Note that similar estimates for the forward angle extrapolation of inelastic transitions have been successful for many other targets.[40–42] In the present work, the derived GOS-dipole forward angle extrapolation, plus or minus 50% (commensurate to the experimental uncertainty on the DCS data), is used as the range of forward angle DCS values in order to calculate realistic uncertainties for the derived ICS. The ICSs derived using the GOS-dipole extrapolation are also presented in Table III. Here, we note that the ICS derived using our standard method are in excellent accord with those values determined using the GOS-dipole extrapolation.

IV. DETAILS OF THE CALCULATION

Pyrimidine, $C_4H_4N_2$, is a diazine that belongs to the C_{2v} point group. It has a dipole moment[43] of 2.334 D and a vertical ionization energy[44] of around 9.73 eV. The spherical polarizability for this molecule[45] is 40–60 a_0^3. Pyrimidine has 42 electrons and its ground state configuration (for simplicity, the orbitals are not listed in energy order) is $(1\text{–}11\ a_1)^{22}$ $(1\text{–}2\ b_1)^4$ $(1\text{–}7\ b_2)^{14}$ $(1a_2)^2$. Its isomer pyrazine (where the nitrogen atoms are in positions 1 and 4 rather than 1 and 3) has been studied in some detail by us:[46] the calculations presented here are based on the experience gained in that work.

Using the optimized geometry of pyrimidine[47] and following our earlier work, we performed calculations with two different basis sets: a compact basis set, cc-pVDZ, and a diffuse one, 6–311+G**. For the static-exchange plus polarization (SEP) calculations presented below, we generated Hartree-Fock (HF) SCF orbitals. For the CC calculations, we performed state-averaged complete active space self-consistent field (SA-CASSCF) calculations using MOLPRO.[48] Again, the averaging scheme was selected following tests performed for pyrazine.[46] In our SA-CASSCF calculations, we chose the active space (10, 8). This active space comprises 10 electrons distributed among the 6 valence π orbitals and the two lone-pair σ orbitals located on the two nitrogen atoms. The doubly occupied core in our calculations is therefore $(1\text{–}10a_1)^{20}$ $(1\text{–}6b_2)^{12}$. This is similar to the choice made for pyrazine.

Table I shows our results for the ground state properties (energy and dipole moment) of pyrimidine. The energy at both HF and CASSCF levels, with both basis sets, is only in fair agreement with more accurate calculations. The dipole moments, on the other hand, are within 10%, with the compact basis set providing results within 1%. Table II shows our calculated vertical excitation thresholds along with an assignment of the states to the measured electron energy loss features (for details of this assignment, see Sec. VI). We also report the data of Ferreira da Silva *et al.*[18] used to classify our experimental cross sections as well as results from the measurements of Fischer *et al.*[29] and the time-dependent (TDDFT) calculations of Stener *et al.*[28] These latter calculations, geared specifically towards providing an accurate description of the excited states, report many more singlet states in the 0–10 eV range than we find in our calculations. Some of these are of Rydberg/partial Rydberg character that is poorly represented by our models, and therefore probably appear at much higher energies. The limited active space we use accounts for the absence of some higher-lying valence states (expanding the active space by several orbitals would make subsequent CC scattering calculations too big to be tractable). It is clear at first sight that both our calculations overestimate the excitation thresholds. Comparing with the results of Fischer *et al.*,[29] the difference is smaller than 0.75 eV for states below 5 eV but increases to more than 1 eV above that energy. The relatively poor match is not surprising and is due to the fairly "simple" (in quantum chemistry terms: small basis set, small active space, and no perturbative corrections) nature of our target calculations.

TABLE I. Energy (in Hartree) and dipole moment (in Debye) of the ground state of pyrimidine calculated at the HF and SA-CASSCF levels, using the basis sets indicated in the table. Also listed are the experimental values of the ground state dipole moment from Blackman *et al.*[43] and the calculated energy derived from Palmer *et al.*[17]

	cc-pVDZ		6–311+G**		
	HF	CASSCF	HF	CASSCF	Acc. value
E	− 262.71	− 262.79	− 262.75	− 262.83	−263.4019
μ	2.31	2.36	2.53	2.53	2.334 ± 0.010

In order to ensure that the electronic density of both the target states and L^2 functions included in the CC expansion is contained inside the R-matrix sphere, we have employed a radius $a = 13a_0$ (and its corresponding continuum GTOs basis set[49]) when using the cc-pVDZ basis set and $a = 18a_0$ (again, with the appropriate continuum basis set[50]) when using the 6–311+G** basis set.

Results for two scattering models are presented in this paper. The simpler is an SEP model that includes in the CC expansion L^2 configurations in which

(a) the scattering electron occupies one of a selected number of virtual (unoccupied in the Hartree-Fock ground state configuration) orbitals and

(b) the core orbitals of the molecule are doubly occupied, but the molecule is allowed to polarize by promoting one electron from the other occupied orbitals to the selected virtual orbitals, which are also available for the scattering electron.

The more sophisticated model that allows us to determine electronic excitation cross sections is based on the close-coupling approximation. In this case, in addition to the ground state of the target, another 28 states are included in the CC expansion together with L^2 configurations in which

(a) the scattering electron occupies one of the orbitals in the active space and

(b) the scattering electron occupies a virtual orbital.

In this model, polarization effects are also accounted for by the inclusion of electronically excited states of the target in the expansion. The SEP model allows us to better represent short range polarization and correlation effects: changing the number of orbitals included in our virtual space allows us to tune these effects.[46] This model is therefore better at providing positions for the low-lying shape resonances in good agreement with experiment, as well as describing a

TABLE II. Vertical excitation energies, calculated at SA-CASSCF level with the indicated basis sets, for the excited electronic states of pyrimidine included in the CC calculation. Also listed are the experimental results of Fischer *et al.*[29] and Ferreira da Silva *et al.*[18] and values from TDDFT calculations by Stener *et al.*[28] The symmetry of the states, the experimental energy loss features (see Figure 1) and spectral assignments are also presented.

	VE energy (eV)						Energy loss spectra	
	This work							
State no.	cc-pVDZ	6–311+G**	Fischer *et al.*[29]	Ferreira da Silva *et al.*[18]	Stener *et al.*[28]	Symmetry	Label	Energy (eV)
1	4.00	3.97	4.0	…	4.45	$1\,^3A_1$	I	4.3
2	4.54	4.54	3.8	…	3.05	$1\,^3B_1$	I	4.3
3	4.99	4.97	4.3	4.183	3.44	$1\,^1B_1$	I	4.3
4	5.12	5.08	4.8		4.50	$1\,^3B_2$	I	4.3
5	5.13	5.09	5.3	5.22(5)	5.44	$1\,^1B_2$	II	5.2
6	5.24	5.29	4.4		3.46	$1\,^3A_2$	I	4.3
7	5.27	5.23	5.1		…	$2\,^3A_1$	II	5.2
8	5.63	5.63	4.8		3.67	$1\,^1A_2$	I	4.3
9	6.45	6.43	5.4		4.20	$2\,^3A_2$	II	5.2
10	6.71	6.67	5.9		4.65	$2\,^1A_2$	III	5.9
11	7.07	7.05	5.7		4.60	$2\,^3B_1$	III	5.9
12	7.23	7.21	6.1	∼6.0	4.89	$2\,^1B_1$	III	5.9
13	7.42	7.37	…		…	$2\,^3B_2$	IV	6.7
14	7.54	7.50	…		…	$3\,^3A_1$	IV	6.7
15	8.07	8.02	…		…	$3\,^3B_2$	IV	6.7
16	8.34	8.27	6.8	6.69(1)	6.35	$2\,^1A_1$	IV	6.7
17	8.53	8.46	…		6.55	$2\,^1B_2$	IV	6.7
18	8.84	8.76	…		7.40	$3\,^1A_1$	V	7.5
19	9.04	9.03	…		…	$3\,^3A_2$	VI	8.3 and 9.2
20	9.20	9.18	…		…	$3\,^1A_2$	VI	8.3 and 9.2
21	9.37	9.33	…		…	$3\,^3B_1$	VI	8.3 and 9.2
22	10.18	10.10	7.6	7.478	7.19	$4\,^1A_1$	V	7.5
23	10.26	10.21	…		…	$4\,^3A_2$	VI	8.3 and 9.2
24	10.26	10.22	…		…	$4\,^3B_1$	VI	8.3 and 9.2
25	10.29	10.22	7.6	7.478	7.42	$3\,^1B_2$	V	7.5
26	10.31	10.30	…		…	$4\,^3B_2$	VI	8.3 and 9.2
27	10.46	10.41	…		7.42	$3\,^1B_1$	V	7.5
28	10.51	10.48	…		7.50	$4\,^1B_2$	V	7.5

Ramsauer-Townsend minimum if present. We chose to use 35/40 virtual orbitals when using the cc-pVDZ basis set and 40/70 virtual orbitals when using the 6–311+G** one, for the SEP/CC calculations, respectively. Details of this choice and how it affects resonances can be found in Refs. 46 and 51.

The behaviour of the scattering electron is described by means of a partial wave expansion. In R-matrix calculations, it is customary to include partial waves up to $l = 4$ or $l = 5$ (the inclusion of higher partial waves increases the computational requirements). This is usually appropriate for molecules with no dipole moment for which the expansion converges rapidly. However, for molecules with a large dipole moment such as pyrimidine, this expansion does not converge in the fixed-nuclei approximation. This lack of convergence is circumvented by means of a "Born correction". We use the program POLYDCS (Ref. 52) to calculate "Born-corrected" elastic differential and integral cross sections. This program calculates the total (differential or integral) cross section in the Born approximation, adds to it the partial cross section calculated *ab initio* (with the R-matrix suite in our case) for partial waves up to l_{max} and then subtracts partial cross sections for $l < l_{max}$ determined within the Born approximation. This approach is very effective as the Born approximation tends to be accurate for high partial waves, for which the projectile does not much penetrate the target electronic cloud. In order to correct the integral inelastic cross sections, we follow the approach of Norcross and Padial.[53]

V. ELASTIC CROSS SECTIONS

Figure 2 shows our calculated elastic DCSs for several scattering energies. Both our SEP (using the compact basis set, and partial waves up to $l = 5$) and CC (using the diffuse basis set and $l \leq 4$) results are presented. The agreement is very good for all four energies for which experimental results[15] are available. At 15 eV, the SEP model provides cross sections in better agreement with experiment, particularly in the 50°–130° range. The oscillatory behaviour of the CC DCS is probably due to the fact that, in calculating the DCS, we are neglecting the majority of open channels; the CC results are very good for 10 eV, but at 12 eV (not shown) they already exhibit this behaviour. Nonetheless, the magnitude of the cross section is similar with both methods at all energies.

Figure 3 shows the comparison between experiment and calculation for the ICS. We present the Born-corrected SEP cross section, appropriate for the comparison with experiment, as well as the (uncorrected) cross sections resulting from the R-matrix calculation both at SEP and CC level all calculated with the compact basis set. The very narrow peaks visible in the SEP cross section above 7 eV correspond mostly to non-physical resonances, a normal feature of SEP calculations that use a multi-configuration description for the N + 1 wavefunction. The peaks below this energy (and those visible in the CC cross section) correspond to physical resonances.[15,19,51] Except for the change in the position of these physical resonances, the SEP and CC approximations produce similar results. In the SEP model, the resonance positions are in reasonable agreement with earlier data:[15,19,54] we

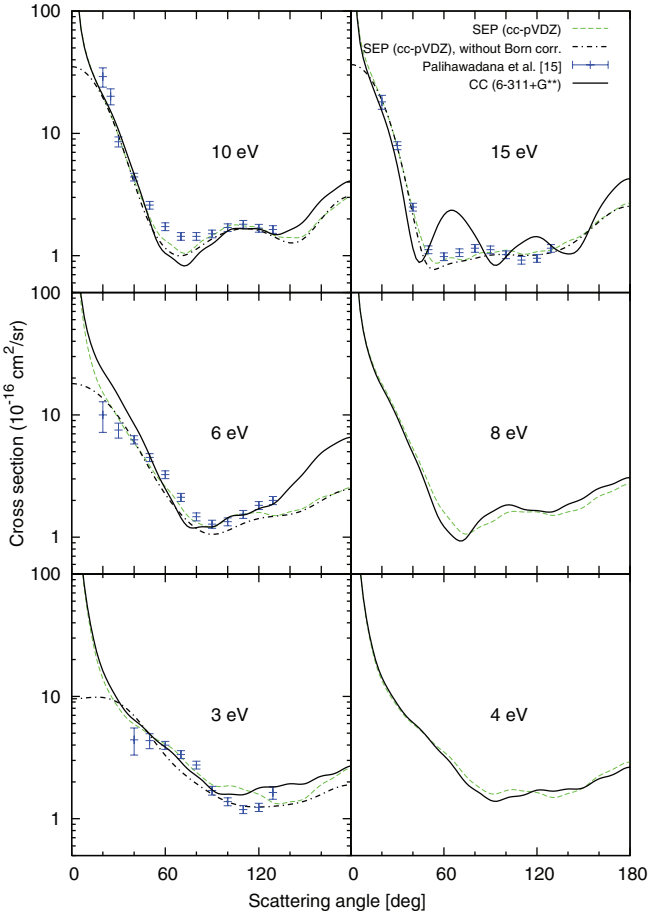

FIG. 2. Elastic differential cross sections for the scattering energies indicated in the panels, at both the SEP (using the compact basis set) and CC (with the diffuse basis set) levels of approximation. Also shown are the experimental results of Palihawadana *et al.*[15] and, for some selected energies, the results obtained from the R-matrix calculation at the SEP level without use of the Born correction.

see a $^2A_2$ resonance at 0.21 eV, a $^2B_1$ resonance at 0.63 eV, and a $^2B_1$ resonance at 5.15 eV. The resonance order is in agreement with Nenner and Schulz;[19] the different order ($^2B_1$, $^2A_2$, $^2B_1$) in the Schwinger calculations of Winstead and McKoy[15] can probably be attributed to the different quality of scattering models used for the different resonant symmetries in their calculations (for a detailed discussion of these resonances, the mixed shape/core excited character of the third resonance and how this is best described in our models, see Refs. 46 and 51).

Despite the excellent agreement of the DCS, the calculated ICS is larger than the experimental one for the whole energy range presented. The Born-corrected theoretical ICS corresponds to integrating the Born-corrected DCS in the whole 0°–180° angular range; in order to obtain the experimental cross section, the results need to be extrapolated before they are integrated. It is this extrapolation that leads to the apparent differences in the ICS. When both experimental and calculated DCS are integrated only in the angular range for which there are measurements (20°–130° for 6 eV and above and 40°–130° below 6 eV), the agreement between theory (Born-corrected) and experiment is, as expected, very good. The comparison for these "partially integrated" results is shown

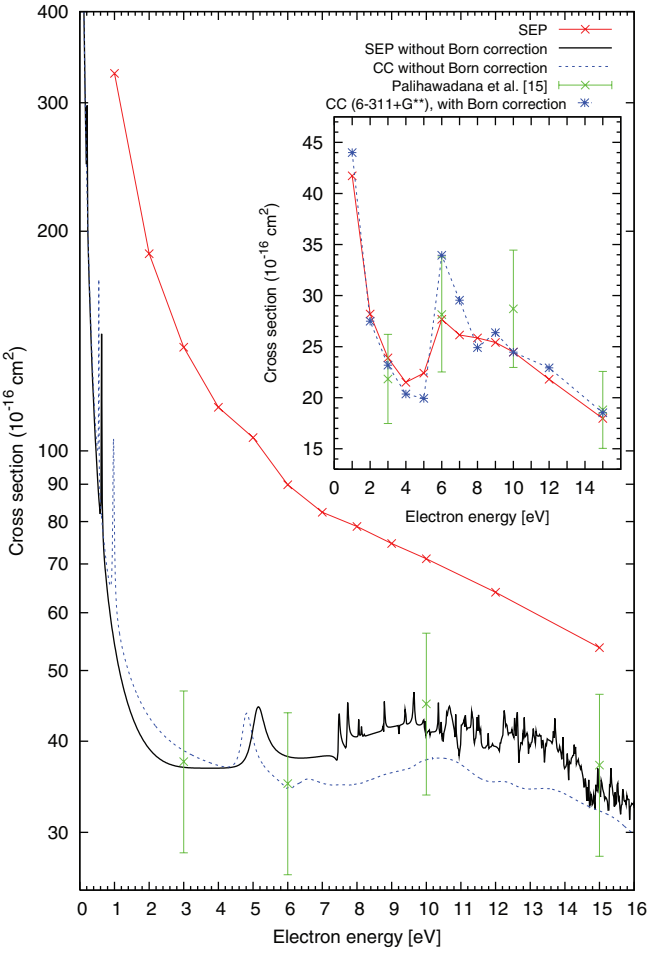

FIG. 3. Elastic integral cross sections at the SEP and CC levels with and without a Born-type correction (the cc-pVDZ basis set was used unless otherwise stated), are compared to the experimental results of Palihawadana *et al.*[15] The inset shows cross sections obtained integrating the calculated and experimental DCS over a restricted angular range (see text for details). Notice the linear scale in this inset.

in the inset in Figure 3: notice that now both the CC and SEP results fall within the error bars of the experiment.

The good agreement between the uncorrected ICS and the experimental results integrated over all angles is no coincidence: as can be seen in Figure 2, the uncorrected R-matrix calculation significantly underestimates the DCS below 10°–20°, a range for which the extrapolation of experimental results is probably also underestimating the DCS. Nonetheless, a more consistent comparison is given by the partial angular integration described above. If this partial integration is performed for the (uncorrected) R-matrix DCS, the results (not shown in the figure) are in slightly poorer agreement with experiment than the corrected ones.

The very encouraging agreement between theory and experiment that we have found for the elastic process, strengthens our confidence in the comparison for the inelastic results.

VI. INELASTIC CROSS SECTIONS

Figure 4 shows our theoretical and experimental results for the total electronically inelastic cross section (TICS). For

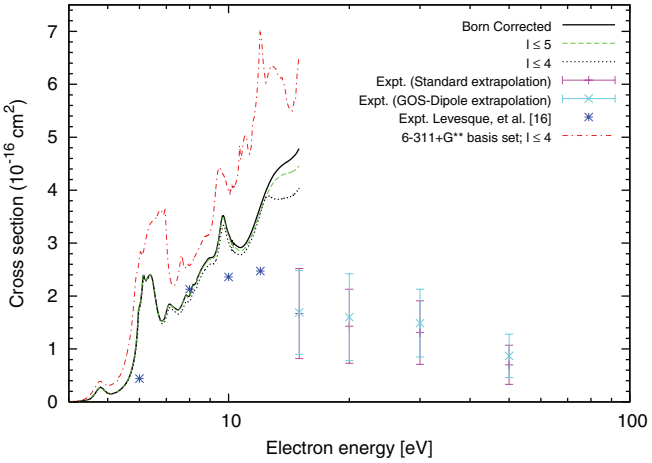

FIG. 4. Integral inelastic cross sections. Calculated results are presented for various models as indicated in the figure; the cc-pVDZ basis set was used unless otherwise stated. Experimental results have been determined as described in Sec. III. Also shown are experimental results for collisions from pyrimidine deposited on an argon substrate from Levesque *et al.*[16]

the calculated data, this means the sum of the cross sections for the 28 excited states included in the CC expansion. Also included in this figure are the corresponding results from experiments with condensed pyrimidine from Levesque *et al.*[16] We present the cross section determined with both the compact and diffuse basis sets: the latter is up to 50% bigger above 10 eV. The structure below this energy corresponds mostly to physical resonances for both calculations. Table III lists the measured cross sections.

A Born correction has been added to the TICS calculated with the compact basis set to account for the partial waves not taken into account in the R-matrix calculation (the increase in the TICS calculated with the diffuse basis set would be similar). It is the corrected cross section that should be compared with experiment. We also show, as an indication of convergence, the uncorrected TICS calculated with partial waves up to both $l = 4$ and $l = 5$.

The agreement for the TICS is excellent up to 10 eV, even if the experimental data have insufficient data points to detect the possible resonances visible in the calculated cross section. For the only energy (15 eV) for which the current experimental and theoretical results are available, the calculations overestimate the total electronically inelastic experimental cross section by about a factor of 3 for the compact basis set and even more for the diffuse one. Given the limitations in both the calculations and experiment, this is probably reasonable agreement. The better agreement with the results of Levesque *et al.*[16] is possibly due to our calculations being more accurate in this lower energy range.

The panels in Figure 5 show the comparison for the inelastic integral cross sections for excitation of states contributing at specific energy loss values. The experiment (like the one on condensed pyrimidine) is unable to determine state-to-state cross sections. However, the behaviour of each spectral feature measured in the energy loss spectra with respect to the incident electron energy and scattering angle (see Figure 1) provides sensitive information that can assist in assigning the origins of the spectral contributions. This information can be

TABLE III. Measured electron impact excitation ICS (10^{-16} cm^2) for pyrimidine. ICS were calculated using a standard extrapolation (SE) or an extrapolation based on the generalised oscillator strength (GOS) behaviour of dipole-allowed transitions. The uncertainty on the data is of the order of 42%–65%. See text for further details.

Experiment		$E_0 = 15$ eV		$E_0 = 20$ eV		$E_0 = 30$ eV		$E_0 = 50$ eV	
Label	E_{loss} (eV)	SE	GOS	SE	GOS	SE	GOS	SE	GOS
I	4.3	0.168	0.165	0.09	0.10	0.054	0.057	0.020	0.025
II	5.2	0.24	0.26	0.12	0.13	0.073	0.083	0.031	0.039
III	5.9	0.11	0.106	0.056	0.061	0.042	0.047	0.017	0.019
IV	6.7	0.23	0.24	0.159	0.154	0.136	0.156	0.071	0.084
V	7.5	0.54	0.55	0.57	0.72	0.54	0.67	0.32	0.45
VI	8.3	0.141	0.140	0.165	0.162	0.156	0.161	0.081	0.086
VI	9.2	0.25	0.23	0.27	0.27	0.31	0.31	0.155	0.164
Sum		1.67	1.69	1.43	1.60	1.31	1.49	0.70	0.87

combined with the theoretical calculations described above, sophisticated calculations from the literature and other experimental results[17,18,28–30] to determine the states that contribute to the cross sections at specific energy loss values (see Sec. III). The present assignments to the experimental spectra are detailed in Table II. These assignments and the comparisons in Figure 5 are now discussed in detail.

For the lower-lying electron energy loss features (at 4.3 eV, 5.2 eV, and 5.9 eV, panels (a), (b), and (c), respectively, in Fig. 5), we find no problems matching our calculated electronic spectrum with the experimental assignments, even though our calculated excitation energies are overestimated. The energy loss feature at 6.7 eV (panel (d) in Figure 5) is associated in the experiment to two states ($2\,^3B_2$ and $2\,^1A_1$). Our calculations, however, produce two triplet states ($3\,^3A_1$ and $3\,^3B_2$) with vertical excitation energies lying between the $2\,^3B_2$ and $2\,^1A_1$ states. Therefore, we also assign these two states to this energy loss feature as well as the $2\,^1B_2$ state; the latter because we include the state $3\,^1B_2$ in the 7.5 eV energy loss feature (see below).

The most intense energy loss feature in the experimental spectra around 7.5 eV (Figure 5(e)) arises from contributions of the $3\,^1A_1$ and $2\,^1B_2$ states, which possess a large oscillator strength.[28] We assume that in our calculations these features are associated to those states, among all those included, that have the largest transition moments with the ground state (−1.96 a.u. and 1.94 a.u., respectively): $4\,^1A_1$ and $3\,^1B_2$. Our calculations find another $^1B_2$ state lying below the $3\,^1B_2$, that appears to have a small oscillator strength[28] and probably does not significantly contribute to the experimental spectra; our assignment of the $3\,^1B_2$ state to this energy loss feature is therefore consistent with the experiment and other calculations. The state of $^1A_1$ symmetry contributing to this energy loss feature was identified by Stener *et al.*[28] as the second excited state of this symmetry but, as stated above, we select the third excited state ($4\,^1A_1$) because it has the largest transition moment; this swap of states is probably due to the limitations of our description of the target excited states. Since the second and third $^1A_1$ excited states were found to lie close in energy in the calculations of Stener *et al.*,[28] we choose to assign the $3\,^1A_1$ state to this energy loss feature as well. In addition, the states $3\,^1B_1$ and $4\,^1B_2$ appear in the calculation of Stener *et al.*[28] at 7.42 eV and 7.50 eV, respectively, and we therefore deem them to contribute to the 7.5 eV feature too. In summary, five states contribute to the cross section associated with $E_{loss} = 7.5$ eV, however, the feature is dominated by the contributions from the dipole-allowed transitions to the $4\,^1A_1$ and $3\,^1B_2$ states.

The highest-lying electron energy loss structures at 8.3 eV and 9.2 eV (Figure 5(f)) are suggested to arise mainly from contributions of the Rydberg states. We compare these with the sum of the calculated cross sections for all the states we cannot assign to the lower-lying energy loss peaks: these are higher lying states (some of which may possess a partial Rydberg character). It is worth mentioning that Ferreira da Silva *et al.*[18] reported a $^1A_1$ valence state at 8.800 eV. This state might correlate with our $5\,^1A_1$ state, which in our case appears above 10.5 eV, and is not included in our scattering calculations.

Looking at Figure 5 we note that the gas and condensed phase experimental results seem to be consistent, with the magnitude of their cross sections being very similar. The calculations produce "partial sum" cross sections that are always bigger than the experimental ones, as one would expect given that the total inelastic cross section is also overestimated by the calculations. The only exception is the cross section interpreted in the experiment as arising from excitation to Rydberg states: where for the other cases, calculations produce results that are as much as 4 times bigger for 15 eV, this cross section is underestimated by a factor of 4. As mentioned above, our calculations do not include the excited state of $^1A_1$ symmetry found in the experiment at 8.8 eV (probably corresponding to the state $7\,^1A_1$ at 8.71 eV in the calculations of Stener *et al.*[28]). The calculated[28] oscillator strength of this state is 5.97, suggesting that its contribution to the inelastic cross section might be non-negligible. Omitting this state from the calculations might well be the reason for the calculated cross section being underestimated here.

The biggest "partial sum" cross section is that for $E_{loss} = 7.5$ eV, for both calculations and measurements; at 15 eV, it contributes 40% to the calculated cross section. It is this and the cross section associated to $E_{loss} = 8.3$ and 9.2 eV that correspond to excitation of the higher lying states. It is conceivable that a better representation of those states will change the cross section for their excitation and therefore reduce the TICS at higher energies.

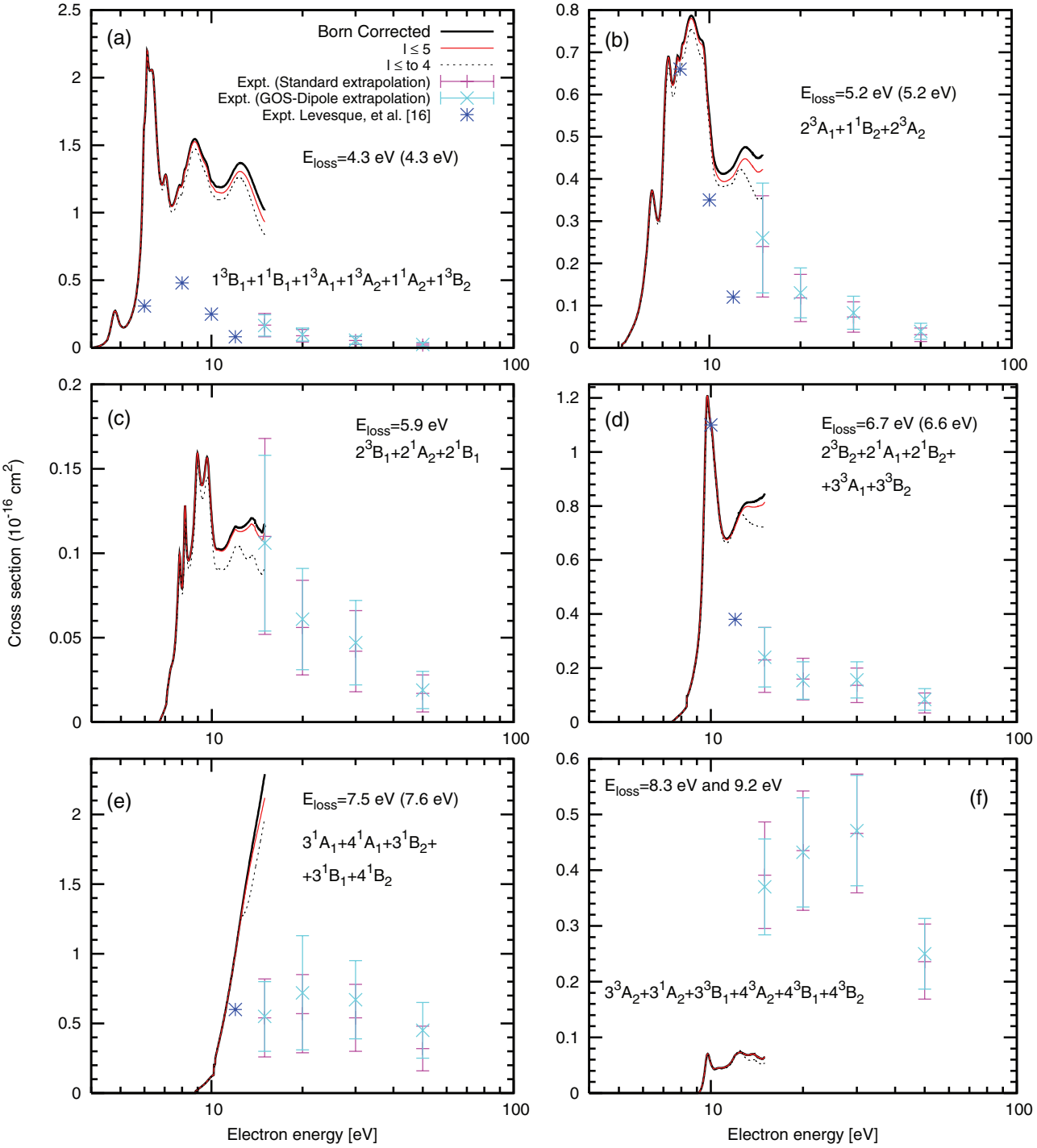

FIG. 5. Integral inelastic cross sections for excitation into the states indicated in the panels. The choice of target states "grouped" together is given by the experiment (see text). The bottom right hand panel shows the calculated cross section for those states included (and energetically open) in our calculation that are not reported in the literature (Stener *et al.*[28] study only states for which transitions are dipole allowed and, in the case of the triplets, only up to 5 eV). The values in brackets correspond to the E_{loss} in the experiments by Levesque *et al.*[16]

It is interesting to note that the agreement with theory both for the TICS and the "partial sum" cross sections, as measured for condensed pyrimidine,[16] is better than that for the gas phase results. In the case of the "partial sum" cross sections, the states grouped together are somewhat different and so this better agreement may therefore be fortuitous. Since most of the states considered are valence, their thresholds are unlikely to change significantly in going from the gas to condensed phase. Usually, the thresholds are lower in the condensed phase; our calculated excitation thresholds are, in most cases higher than those reported by both experiments and accurate calculations as shown in Table II. We have consequently performed calculations in which we have shifted the excitation thresholds to the values determined by Fischer *et al.*: we observed only small differences in both the TICS and the "partial sum" cross sections.

VII. CONCLUSIONS

Experimental and theoretical studies of electronically inelastic electron scattering and theoretical studies of elastic scattering from pyrimidine have been performed. For the only overlapping energy (15 eV), agreement between measured and calculated inelastic cross sections is quite fair, particularly when one allows for the very difficult nature of the calculations and measurements. This comparison has been performed both for the total (summed) inelastic cross section and for "partial sum" cross sections for excitation into groups of states. The present calculations for various models (basis sets and levels of approximation) also provide integral and differential elastic cross sections in very good agreement with prior experimental results. That result gave us confidence in attempting the electronic state excitation cross section calculations we have reported. With the results obtained from the work contained in this paper, and those from previous studies,[14,15,20] we believe it is now plausible to construct a database that might be employed in studying charged particle tracks through gaseous pyrimidine. This, like in earlier studies on water,[55,56] represents a first step for elucidating radiation damage in our body by using pyrimidine as a prototype DNA/RNA moiety.

A more accurate description of the excited states of the target is needed in the theoretical work, in order to produce more accurate inelastic cross sections. The difficulty in achieving that, however, should not be underestimated.

ACKNOWLEDGMENTS

This work was supported by the EPSRC. The work at Flinders University was supported by the ARC through its Centres of Excellence Program. M.J.B. also acknowledges the University of Malaya for his "Distinguished Visiting Professorship."

[1] M. J. Brunger and S. J. Buckman, Phys. Rep. **357**, 215 (2002).
[2] T. N. Resigno, C. W. McCurdy, A. E. Orel, and B. H. Lengsfield III, in *Computational Methods for Electron Molecule Collisions*, edited by W. M. Huo and F. A. Gianturco (Plenum, New York, 1995), pp. 1–44.
[3] C. Winstead and V. McKoy, Comput. Phys. Commun. **128**, 386 (2000).
[4] R. F. da Costa, F. J. da Paixão, and M. A. P. Lima, J. Phys. B: At. Mol. Opt. Phys. **37**, L129 (2004).
[5] R. F. da Costa, F. J. da Paixão, and M. A. P. Lima, J. Phys. B: At. Mol. Opt. Phys. **38**, 4363 (2005).
[6] P. G. Burke, *R-Matrix Theory of Atomic Collisions: Application to Atomic, Molecular and Optical Processes* (Springer, 2011).
[7] P. A. Thorn, M. J. Brunger, H. Kato, M. Hoshino, and H. Tanaka, J. Phys. B: At. Mol. Opt. Phys. **40**, 697 (2007).
[8] B. Boudaïffa, P. Cloutier, D. Hunting, M. A. Huels, and L. Sanche, Science **287**, 1658 (2000).
[9] L. Sanche, Eur. Phys. J. D **35**, 367 (2005).
[10] I. Baccarelli, I. Bald, F. A. Gianturco, E. Illenberger, and J. Kopyra, Phys. Rep. **508**, 1 (2011).
[11] M. Michaud, M. Bazin, and L. Sanche, Int. J. Radiat. Biol. **88**, 15 (2012).
[12] A. Dora, J. Tennyson, L. Bryjko, and T. van Mourik, J. Chem. Phys. **130**, 164307 (2009).
[13] C. Winstead and V. McKoy, J. Chem. Phys. **125**, 174304 (2006).
[14] J. B. Maljković, A. R. Milosavljević, F. Blanco, D. Šević, G. García, and B. P. Marinković, Phys. Rev. A **79**, 052706 (2009).
[15] P. Palihawadana, J. P. Sullivan, M. J. Brunger, C. Winstead, V. McKoy, G. García, F. Blanco, and S. J. Buckman, Phys. Rev. A **84**, 062702 (2011).
[16] P. L. Levesque, M. Michaud, and L. Sanche, J. Chem. Phys. **122**, 094701 (2005).
[17] M. H. Palmer, I. C. Walker, M. F. Guest, and A. Hopkirk, Chem. Phys. **147**, 19 (1990).
[18] F. Ferreira da Silva, D. Almeida, G. Martins, A. R. Milosavljevic, B. P. Marinkovic, S. V. Hoffmann, N. J. Mason, Y. Nunes, G. García, and P. Limão Vieira, Phys. Chem. Chem. Phys. **12**, 6717 (2010).
[19] I. Nenner and G. J. Schulz, J. Chem. Phys. **62**, 1747 (1975).
[20] A. Zecca, L. Chiari, G. García, F. Blanco, E. Trainotti, and M. J. Brunger, J. Phys. B: At. Mol. Opt. Phys. **43**, 215204 (2010).
[21] J. D. Gorfinkiel and J. Tennyson, J. Phys. B: At. Mol. Opt. Phys. **38**, 1607 (2005).
[22] J. Tennyson, Phys. Rep. **491**, 29 (2010).
[23] P. Burke and K. Berrington, *Atomic and Molecular Processes: An R-Matrix Approach* (IOP, Bristol, 1993).
[24] J. M. Carr, P. Galiatsatos, J. Gorfinkiel, A. Harvey, M. Lysaght, D. Madden, Z. Mašín, M. Plummer, J. Tennyson, and H. Varambhia, Eur. Phys. J. D. **66**, 1 (2012).
[25] In our implementation, the L^2 functions defined below should also be contained inside the sphere.
[26] More accurately, it is the matrix obtained from the sum of the Hamiltonian and the Bloch operator[6] that is diagonalized.
[27] M. J. Brunger and P. J. O. Teubner, Phys. Rev. A **41**, 1413 (1990).
[28] M. Stener, P. Decleva, D. M. P. Holland, and D. A. Shaw, J. Phys. B: At. Mol. Opt. Phys. **44**, 075203 (2011).
[29] G. Fischer, Z.-L. Cai, J. R. Reimers, and P. Wormell, J. Phys. Chem. A **107**, 3093 (2003).
[30] Y. J. Li, J. Wan, and X. Xu, J. Comput. Chem. **28**, 1658 (2007).
[31] M. Nooijen, Spectrochim. Acta A **55**, 539 (1999).
[32] M. Allan, J. Phys. B: At. Mol. Opt. Phys. **38**, 3655 (2005).
[33] D. B. Jones, S. M. Bellm, P. Limão Vieira, and M. J. Brunger, "Low-energy electron scattering from pyrimidine: Similarities and differences with benzene," Chem. Phys. Lett. (in press).
[34] Y. Itikawa, J. Phys. B: At. Mol. Opt. Phys. **37**, R1 (2004).
[35] L. Campbell, M. J. Brunger, A. M. Nolan, L. J. Kelly, A. B. Wedding, J. Harrison, P. J. O. Teubner, D. C. Cartwright, and B. McLaughlin, J. Phys. B: At. Mol. Opt. Phys. **34**, 1185 (2001).
[36] A. Faure, J. D. Gorfinkiel, and J. Tennyson, J. Phys. B: At. Mol. Opt. Phys. **37**, 801 (2004).
[37] E. N. Lassettre, J. Chem. Phys. **43**, 4479 (1965).
[38] A. R. P. Rau and U. Fano, Phys. Rev. **162**, 68 (1967).
[39] L. Vriens, Phys. Rev. **160**, 100 (1967).
[40] Z. Chen and A. Z. Msezane, J. Mol. Struc.: THEOCHEM **529**, 55 (2000).
[41] P. A. Thorn, M. J. Brunger, P. J. O. Teubner, N. Diakomichalis, T. Maddern, M. A. Bolorizadeh, W. R. Newell, H. Kato, M. Hoshino, H. Tanaka, H. Cho, and Y.-K. Kim, J. Chem. Phys. **126**, 064306 (2007).
[42] H. Kato, M. Hoshino, H. Tanaka, P. Limão Vieira, O. Ingolfsson, L. Campbell, and M. J. Brunger, J. Chem. Phys. **134**, 134308 (2011).
[43] G. L. Blackman, R. D. Brown, and F. R. Burden, J. Mol. Spectrosc. **35**, 444 (1970).
[44] N. Hush and A. S. Cheung, Chem. Phys. Lett. **34**, 11 (1975).
[45] "NIST Standard Reference Database Number 101," 2011.
[46] Z. Mašín and J. D. Gorfinkiel, J. Chem. Phys. **135**, 144308 (2011).
[47] M. Schreiber, M. R. Silva-Junior, S. P.A. Sauer, and W. Thiel, J. Chem. Phys. **128**, 134110 (2008).
[48] H.-J. Werner, P. J. Knowles, R. Lindh, F. R. Manby, M. Schütz *et al.*, MOLPRO, version 2009.1, a package of *ab initio* programs 2009, see http://www.molpro.net.
[49] A. Faure, J. D. Gorfinkiel, L. A. Morgan, and J. Tennyson, Comput. Phys. Commun. **144**, 224 (2002).
[50] M. Tarana and J. Tennyson, J. Phys. B: At. Mol. Opt. Phys. **41**, 205204 (2008).
[51] Z. Mašín and J. D. Gorfinkiel, "Shape and core excited resonances in electron collisions with diazines" (unpublished).
[52] N. Sanna and F. A. Gianturco, Comput. Phys. Commun. **114**, 142 (1998).
[53] D. W. Norcross and N. T. Padial, Phys. Rev. A **25**, 226 (1982).
[54] A. Modelli, P. Bolognesi, and L. Avaldi, J. Phys. Chem. A **115**, 10775 (2011).
[55] A. Muñoz, F. Blanco, G. García, P. A. Thorn, M. J. Brunger, J. P. Sullivan, and S. J. Buckman, Int. J. Mass Spectrom. **277**, 175 (2008).
[56] A. G. Sanz, M. C. Fuss, A. Muñoz, F. Blanco, P. Limão Vieira, M. J. Brunger, S. J. Buckman, and G. García, Int. J. Radiat. Biol. **88**, 71 (2012).